



Low power femtosecond tip-based nanofabrication with advanced control

Jiangbo Liu¹ · Zhixiong Guo¹ · Qingze Zou¹

Received: 9 October 2017 / Accepted: 12 January 2018
© Springer-Verlag GmbH Germany, part of Springer Nature 2018

Abstract

In this paper, we propose an approach to enable the use of low power femtosecond laser in tip-based nanofabrication (TBN) without thermal damage. One major challenge in laser-assisted TBN is in maintaining precision control of the tip–surface positioning throughout the fabrication process. An advanced iterative learning control technique is exploited to overcome this challenge in achieving high-quality patterning of arbitrary shape on a metal surface. The experimental results are analyzed to understand the ablation mechanism involved. Specifically, the near-field radiation enhancement is examined via the surface-enhanced Raman scattering effect, and it was revealed the near-field enhanced plasma-mediated ablation. Moreover, silicon nitride tip is utilized to alleviate the adverse thermal damage. Experiment results including line patterns fabricated under different writing speeds and an “R” pattern are presented. The fabrication quality with regard to the line width, depth, and uniformity is characterized to demonstrate the efficacy of the proposed approach.

1 Introduction

Surface nanopatterning is of paramount importance in nanotechnology. Chemical vapor deposition [1], electron beam lithography [2], tip-based nanomanufacturing (TBN) [3, 4], and near-field optical lithography [5–7] are among the approaches intensively studied in recent years. Each of these techniques has its own features as reported (see recent reviews [7–9]). Nevertheless, there is a pressing need to develop a high-quality, high-speed nanomanufacturing technique to achieve precision, uniform, flexible, and large-size nano-patterning on a variety of different types of samples.

The advent of ultrashort pulsed (USP) lasers opened a new horizon for micro/nanomanufacturing. In particular, plasma-mediated ablation occurs when the laser incident heat flux is over the threshold for optical breakdown [10]. In the ultrafast time regime, plasma expansion happens on a

timescale smaller than the time of heat transfer to the lattice, and thermal damages are reduced or eliminated [11]. Furthermore, the substantial plasma generation and absorption enables the ablation of materials (e.g., transparent or low absorption materials) that are normally difficult to ablate via continuous wave or other types of pulsed lasers [12–14]. Thus, efficient processing of a vast spectrum of different materials via the USP laser plasma-mediated ablation is possible. These distinct features make USP laser a promising tool for micro/nanofabrication. Due to the optical diffraction limit, however, direct writing with USP laser is usually restricted to micromachining. Nanoscale patterning might be achieved if the threshold intensity for ablation can be well controlled to occur only in a nano vicinity [15, 16].

Near-field optics has been exploited to overcome the diffraction limit. An easy and flexible approach is to focus the laser radiation down to a few nanometers region via near-field technologies, e.g., scanning tunneling microscopy (STM) or atomic force microscopy (AFM) [17, 18]. In the so-called surface-enhanced Raman spectroscopy (SERS) effect, a 10^6 intensity enhancement can be attained on conductive surface in the near-field beneath the tip, using a laser to externally illuminate the tip via laser radiation. Efficient intensity enhancement can also be achieved on silicon AFM tips, although the enhancement becomes much weaker in dielectric tips. The SERS has been attributed to an interplay

✉ Qingze Zou
qzzou@soe.rutgers.edu
Jiangbo Liu
jiangbo.liu@rutgers.edu
Zhixiong Guo
guo@jove.rutgers.edu

¹ Department of Mechanical and Aerospace Engineering, Rutgers, The State University of New Jersey, Piscataway, NJ 08854, United States

of electrostatic, surface plasmon, and electromagnetic resonance effects.

There are still challenges in achieving uniform, productive, and large-range nano-patterning using laser-assisted TBN (LA-TBN) ablation techniques. Specifically, one of the major challenges is to accurately control the tip-sample spacing in both the lateral and vertical directions throughout the LA-TBN process, for the tip-sample spacing can be adversely affected by the environmental disturbances, variations in the fabrication condition, and the vibrational dynamics and hysteresis behaviors of the piezoelectric actuator system. Therefore, usually high-power USP laser is employed to alleviate the required tip-sample positioning accuracy. The use of strong USP laser, however, can burn the STM/AFM tips easily. To this end, we propose to use a relatively low-power USP laser system that is conventionally used for diagnostics applications. To reduce the tip thermal expansion effect that limits the reliability and resolution of TBN [19], silicon nitride (Si_3N_4) cantilever probes that are thermally stable with small thermal expansion are used. To achieve highly productive and uniform nanostructuring, advanced control techniques such as the modeling-free iterative learning control [20] are utilized to control the motion and positioning of the tip during the fabrication process. The near-field enhanced intensity beneath the AFM tip apex is stably maintained throughout the entire fabrication process, such that the near-field intensity exceeds the optical breakdown threshold of the sample material while the tip is “writing” the pattern. As a result, a uniform pattern can be produced.

2 Experiment setup

The experimental setup, as schematically depicted in Fig. 1, consists of four major parts: a USP laser, a beam delivery and focusing system, an AFM system, and a data acquisition (DAQ) and control system. The USP laser is a Spectra-Physics Tsunami mode-locked Ti:sapphire system pumped by a Millennia V laser with a tunable wavelength range of 710–830 nm, and in this study the wavelength was chosen at 760 nm. The pulse width was 80 fs with repetition rate of 80 MHz, and the output power was measured at 640 mW. The beam is delivered by a few reflection mirrors and finally

focused to the AFM tip apex by a diverging lens ($D = 18$ mm, $f = 100$ mm, $NA = 0.09$), followed by a converging lens ($D = 18$ mm, $f = 250$ mm, $NA = 0.036$). The focused spot size was measured around 20 μ m in diameter. The power of the laser beam after going through all the mirrors and lenses was measured at ~ 520 mW. The incidence angle was 3–5° (with respect to the horizontal baseline). In the AFM system (Dimension ICON, Bruker-Nano Inc.), piezoelectric actuators were used to generate the 3-D motion of the tip (see Table 1 for the specifics of the tip), and a computer control system (a Matlab-xPC-target control system) was utilized to control the piezo actuators through a DAQ system (PCI-6259, Nation Instrument, Inc). Two manual motion stages were installed to adjust each of the focusing lenses in x – y directions, so that the laser spot can be finely tuned to be focused at the interface between the AFM tip and the sample surface.

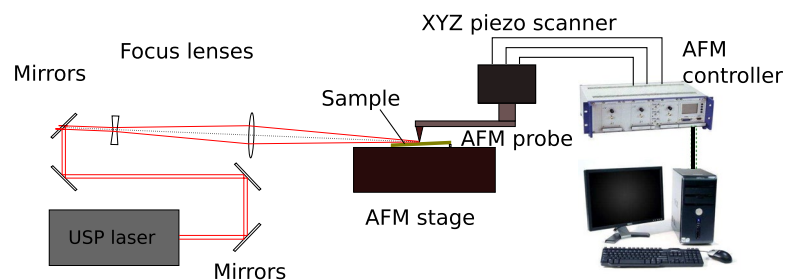
The sample employed in the experiment was a gold film (~ 100 nm in depth) deposited on a silicon substrate. The sample was installed on the AFM sample stage with a tilt angle around 3–5° (with respect to the horizontal baseline) facing the laser incidence direction. Thus, the incidence angle of the laser was around 80–84° (with respect to the normal direction of the sample).

During the entire fabrication process, the laser pulses were continuously focused onto the AFM tip, and the position of the tip was well controlled to maintain a minimal stable tip-sample contact, by monitoring and maintaining the deflection signal (i.e., the contact force between the tip and sample) around the minimal value via feedback control. By positioning the AFM tip near the center of the laser spot, and driving the tip to accurately follow the desired pattern of which the total range was within the spot size of the focused

Table 1 The parameters of AFM probe

Tip material	Silicon nitride
Tip radius	5–12 nm
Length of cantilever	27 μ m
Tip side angle	17.5°
Tip front angle	25°
Tip back angle	15°

Fig. 1 Schematic of the experimental setup



laser beam, arbitrary 2D pattern can be fabricated. Tracking of arbitrary given desired trajectory (i.e., desired pattern shape) within a relatively large area of $34\ \mu\text{m} \times 34\ \mu\text{m}$ was achieved by using the modeling-free inversion-based iterative control (MIIC) technique [20], with the tracking precision error around the sensor noise level.

3 Results and discussion

The AFM images of the line patterns fabricated under eight different “writing” speeds (i.e., the lateral velocity) are shown in Fig. 2a, b, respectively, where the “writing” speed of each line was doubled from that to its right, from $0.2\ (25/2^7)\ \mu\text{m/s}$ for the most right line to $25\ \mu\text{m/s}$ for the most left line, respectively. The mean and standard deviation of the depths, widths and uniformity (measured by the relative length extension of each patterned line (curve) relative to the length of the desired reference line) of each fabricated line were quantified, where the uniformity was quantified as

$$r = (l_i - l_r) / l_r \times 100\%, \tag{1}$$

with l_i and l_r the length of the center curve of the i th patterned line and the desired reference line, respectively. The results are shown as in Fig. 3a–c, respectively. As can be seen from Fig. 2, all the lines fabricated were very smooth and straight in general. Such a high uniformity of the line patterns was also confirmed by the depth, width, and uniformity quantified. Among all the eight lines fabricated, the relative variation of the depth and width variation were within 18.5 and 7.6%, respectively. Also as shown in Figs. 2 and 3, the (mean) width and depth of the patterned lines decreased in general as the patterning speed increased, from $76.3\ \text{nm}$ and $12.5\ \text{nm}$ to $55.4\ \text{nm}$ and $1.6\ \text{nm}$, respectively. As noticed, both the depth and width of the lines saturate as the patterning/writing speed reduced to $0.2\ (25/2^7)\ \mu\text{m/s}$. However, the relative extension of the line remained largely the same across all the patterning speeds, except the last

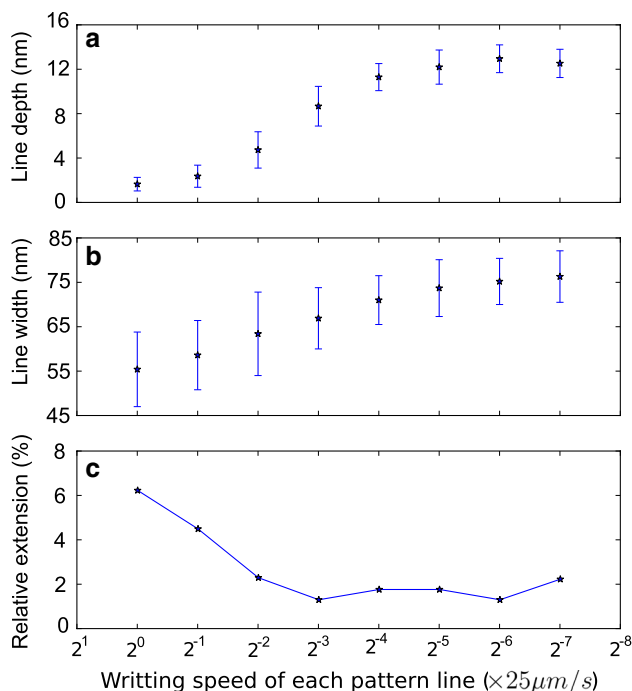
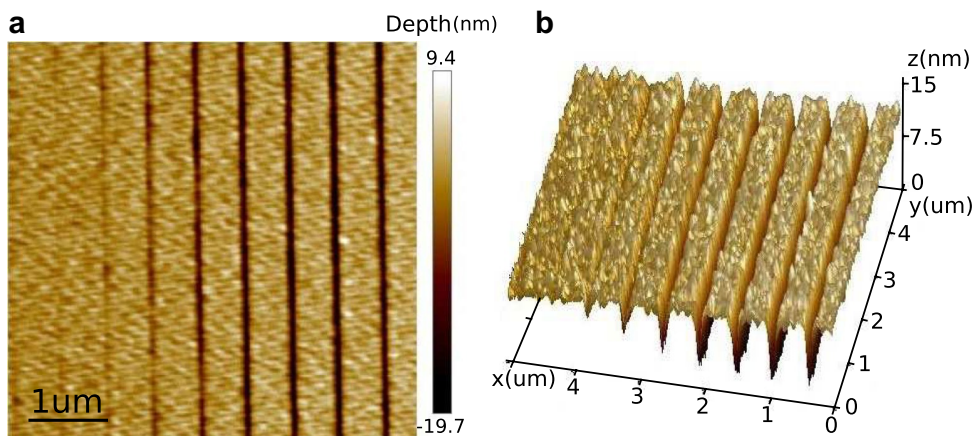


Fig. 3 The width (a), depth (b), and uniformity (c) of each fabricated line vs. the lateral writing speed, where the vertical bar denotes the standard deviation measured at each speed

two highest speeds (the first two data points on the left in Fig. 3c), where relatively larger line extension appeared in the quantification. But that was mainly caused by the lines fabricated becoming too shallow (see Fig. 2a) due to the insufficient power for generating ablation, and thereby rendering it difficult to identify the center of the lines.

The above observed line width and depth reduction with the writing speed decrease manifested the effect of writing speed on the duration of laser irradiation, thereby the incidence energy departed to the focused sample area during the writing. As writing speed increased, the laser irradiation fluence per unit lateral writing distance decreased, and

Fig. 2 a AFM (height) image of the line 2D patterns fabricated using eight different patterning (“writing”) speeds (from $0.2\ (25/2^7)\ \mu\text{m/s}$ (the most right line) to $25\ \mu\text{m/s}$ (the most left line), and; b The corresponding 3D view of the line patterns



thereby the width and depth of the fabricated line decreased and became nearly invisible, due to the insufficient fluence to generate ablation when the speed became too high (e.g., at a writing speed of 25 μm/s as in this work). As the laser irradiation in the vicinity of the tip apex typically decreases with the increase of the distance to the tip apex, the tip motion in the vertical direction can be obstructed by the materials around the tip as the line depth becomes larger, and also the laser irradiation on the tip can be blocked/interfered by the materials on both sides of the deep line concave, and the depth of the lines becomes saturated when the motion speed decreases to some point.

The measurement uncertainty can be affected by various factors, including the quantification of the line depth/width, the roughness of the sample surface, the interaction between the tip, the sample surface, the laser power distribution, and other environmental variations. Specifically, the standard deviation of the line depth decreased as the writing speed was increased (see Fig. 3a). Such a reduction is due to the reduction of the laser deposited energy (as the writing speed increased), resulting in much smaller line depth—as the writing speed was increased from 0.2 (25/2⁷) to 25 μm/s, the line depth reduced by over eight times to only 1.5 nm at the speed of 0.2 (25/2⁷) μm/s. However, the relative standard deviation of line depth, i.e., the standard deviation with respect to the mean value of the line depth, was indeed increased with the writing speed increase (from 11% at 0.2 (25/2⁷) to 26% at 25 μm/s). On the contrary, the standard deviation of both the line depth and line width remained largely unchanged (i.e., saturated) as the writing speed was lower than 1.6 (25/2⁴) μm/s. Such a saturation was because the laser beam width has a Gaussian distribution, i.e., the laser power is stronger at the center and weaker at the edge, and the laser ablation in the writing process has a threshold value. Thus, when the writing speed slowed down and the effective beam width reached and exceeded the saturated value, the fabricated lines, i.e., the line width and depth, remained largely unchanged, and so were the standard deviations.

Near-field enhancement Laser radiation in the near field of a tip can be enhanced significantly by the SERS effect [9, 17]. To quantify the SERS enhancement effect in this experiment, we consider the interaction of a laser beam with the tip of the AFM probe as a spheroid under the laser irradiation. The enhancement effect between a tiny dielectric spheroid and a flat sample surface has been well studied in the literature, and many numerical and analytic methods have been proposed. Specifically, the enhancement factor (i.e., the ratio between the enhanced intensity and the incident intensity of the laser beam) can be expressed as [17]:

$$\rho = \left(\frac{\epsilon}{1 + (\epsilon - 1)A} \right)^2, \tag{2}$$

where ϵ is the dielectric constant of the material, and A is a geometry-dependent constant given as

$$A = \frac{ab^2}{2} \int_0^\infty \frac{d\xi}{(a^2 + \xi)^{\frac{3}{2}}(b^2 + \xi)}, \tag{3}$$

with a and b the axis lengths of the equivalent spheroid to the AFM tip, respectively. The dielectric constant of Si_3N_4 is 7.5 and we estimated for the AFM probe used in this experiment, $a = 20\text{--}50$ nm, and $b = 5\text{--}12$ nm, then the estimated intensity enhancement factor is in the range of 10.0–43.9 (10.0 for $a = 20$ nm, $b = 12$ nm; 43.9 for $a = 50$ nm, $b = 5$ nm).

Note that the breakdown threshold of gold film on fused silica was reported at around 1.25×10^{11} W/cm² [19]. However, without the near-field enhancement, the peak irradiation flux of the USP laser used in this experiment at the focus is calculated as 5×10^{10} W/cm²—only about 40% of the threshold value. This implied no ablation when there is no enhancement underneath the tip apex. In fact, after the near-field SERS enhancement, the laser incident flux is increased to the range of $5\text{--}22 \times 10^{11}$ W/cm² (5×10^{11} W/cm² for $a = 20$ nm, $b = 12$ nm; 22×10^{11} W/cm² for $a = 50$ nm, $b = 5$ nm), well above the threshold value for the gold film. Thus, in this experiment the plasma-mediated ablation on the sample beneath the tip can be generated.

The above analysis implies that the laser intensity in the vicinity of the Si_3N_4 tip apex was enhanced to the level of its peak flux over the gold-film threshold for optical break. As for the Si_3N_4 material, the damage threshold is much greater than the gold damage threshold and was measured over 10^{12} W/cm² [21]. In our experimental tests, only minor wearing damage to the Si_3N_4 tip caused by the sliding of the tip on the sample was observed. Thus, the nanopatterning of the gold-film sample beneath the tip apex obtained in this study can be attributed to the plasma-mediated ablation resulting from the near-field SERS enhancement, and our study showed that by keeping the enhanced intensity field between the threshold value of the sample substrate (e.g., gold) and that of the probe tip (e.g., Si_3N_4), nano-patterns on the targeted film can be fabricated without inducing the ablation-caused probe tip damage. This idea provides the avenue for using a weak USP laser along with a dielectric tip in TBN applications.

Thermal expansion We examined the temperature rise due to continuous irradiation of pulses to the tip during the fabrication process from the thermal equilibrium viewpoint. At thermal equilibrium, the absorbed energy rate is balanced by the energy dissipation rate that includes heat conduction, convection, and radiation. For an AFM probe, heat conduction is the dominant mechanism for energy dissipation, and radiation and convection are negligible. In such a scenario, the steady-state heat balance is

$$-k \frac{dT}{dx} = I_0(x), \tag{4}$$

in which k is the thermal conductivity that is 27 W/(mK) for Si_3N_4 . $I_0(x)$ is the incident laser intensity, following a Gaussian profile as

$$I_0(x) = \frac{2P(1-R)}{\pi r^2} e^{-\frac{2x^2}{r^2}}, \tag{5}$$

where P is the incident laser power (= 520 mW), r is the focus spot radius (= 10 μm), and R is the reflectivity of the tip. The temperature difference between the tip apex and any distance at x is then integrated as

$$T_0(0) - T_0(x) = \frac{P(1-R)}{\sqrt{2\pi}rk} \text{erf}\left(-\frac{\sqrt{2}x}{r}\right). \tag{6}$$

As the distance from the tip x increases to a large value, the error function approaches unity and the temperature approaches the initial value. Thus, the temperature rise at the tip apex under continuous irradiation is

$$\Delta T_p = \frac{P(1-R)}{\sqrt{2\pi}rk}. \tag{7}$$

In the present study, surface reflection was negligible because the generation of the plasma cloud was considered to absorb all the incident radiation; thus, $R = 0$. With the present setup values, the tip apex temperature rise was predicted as 768 K, i.e., the tip temperature was 793 °C. This temperature was much below the melting temperature of Si_3N_4 at 1900 °C. Thus, there was no direct thermal damage to the tip during the nanomanufacturing process.

As such, in this study the amount of thermal expansion in the tip due to the temperature increase was small, as the thermal expansion coefficient of Si_3N_4 is very small ($3.3 \times 10^{-6} \text{ K}^{-1}$). Moreover, as the tip-sample vertical positioning was maintained by using a feedback control system, the thermally induced deformation was further compensated for. Therefore, thermal expansion was a minor and negligible issue of ablation in this study.

4 Nano-patterning with control

We further demonstrated that with advanced control techniques, arbitrary patterning can be achieved. In the patterning experiment, the following modeling-free inversion-based iterative learning control (MIIC) algorithm was implemented to obtain the control inputs to the x and y axes piezoactuators of the AFM system to achieve accurate tracking of the desired trajectory (desired pattern) in the lateral x - y axes [20]:

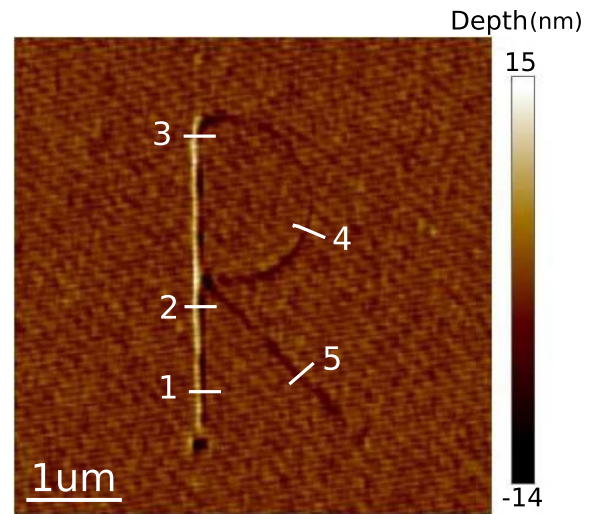


Fig. 4 AFM (height) image of the fabricated “R” pattern (writing speed: 0.2 $\mu\text{m/s}$)

Table 2 Length and depth measured at the five points of the “R” pattern

	Width (nm)	Depth (nm)
Point 1	61	5.0
Point 2	72	6.5
Point 3	82	4.8
Point 4	95	5.5
Point 5	85	4.5
Average	79.0	5.3
Standard deviation	13.0	0.8

$$U_i(j\omega) = U_{i-1}(j\omega) + \frac{U_{i-1}(j\omega)}{Y_{i-1}(j\omega)} (Y_d(j\omega) - Y_{i-1}(j\omega)), \tag{8}$$

where $U_i(j\omega)$, $Y_i(j\omega)$ and $Y_d(j\omega)$ denote the i^{th} iteration input, output, and the desired output in the frequency domain, respectively. In addition, a well-tuned feedback loop was utilized to control the z-piezoactuator, so that the contact force between the tip and sample was maintained at the minimum level.

A pattern of character “R” (as shown in Fig. 4) was obtained at a relatively low speed (0.2 $\mu\text{m/s}$) using the MIIC control technique, and the length and depth of the line measured at randomly chosen positions are shown in Table 2. The depth and width of the “R” pattern were at $5.3 \pm 0.8 \text{ nm}$ and $79.0 \pm 13.0 \text{ nm}$, respectively (see Table 2). It was also observed that the curve of the character, although still very smooth, was not as uniform as the line pattern in Fig. 2. This might be caused by both the change of the contact angle of the tip and the laser incidence angle during the curve patterning. Therefore, the experimental results demonstrated

that arbitrary pattern can be obtained using the proposed approach.

Acknowledgements This material is based on work supported by the National Science Foundation under Grant no. CMMI-1200557.

References

1. S.G. Im, P.J. Yoo, P.T. Hammond, K.K. Gleason, *Adv. Mater.* **19**, 2863–2867 (2007)
2. C. Vieu, F. Carcenac, A. Pepin, Y. Chen, M. Mejjias, A. Lebib, L. Manin-Ferlazzo, L. Couraud, H. Launois, *Appl. Surf. Sci.* **164**, 111–117 (2000)
3. J.R. Felts, K. Kjoller, M. Lo, C.B. Prater, W.P. King, *ACS Nano* **6**, 8015–8021 (2012)
4. H. Wang, Q. Zou, *Tip-Based Nanofabrication* (Springer, New York, 2011), pp. 325–355
5. C.P. Grigoropoulos, D.J. Hwang, A. Chimmalgi, *MRS Bull.* **32**, 16–22 (2007)
6. W. Srituravanich, N. Fang, C. Sun, Q. Luo, X. Zhang, *Nano Lett.* **4**, 1085–1088 (2004)
7. L. Li, M. Hong, M. Schmidt, M. Zhong, A. Malshe, B. Huis, V. Kovalenko, *CIRP Ann. Manuf. Technol.* **60**, 735–755 (2011)
8. A. Malshe, K. Rajurkar, K. Virwani, C. Taylor, D. Bourell, G. Levy, M. Sundaram, J. McGeough, V. Kalyanasundaram, A. Samant, *CIRP Ann. Manuf. Technol.* **59**, 628–651 (2010)
9. P.L. Stiles, J.A. Dieringer, N.C. Shah, R.P. Van Duyne, *Annu. Rev. Anal. Chem.* **1**, 601–626 (2008)
10. M.H. Niemz, E.G. Klancnik, J.F. Bille, *Lasers Surg. Med.* **11**, 426–431 (1991)
11. H. Huang, Z. Guo, *J. Micromech. Microeng.* **19**, 055007 (2009)
12. Y. Liu, S. Sun, S. Singha, M.R. Cho, R.J. Gordon, *Biomaterials* **26**, 4597–4605 (2005)
13. R.R. Gattass, E. Mazur, *Nat. Photon.* **2**, 219–225 (2008)
14. H. Huang, Z. Guo, *J. Phys. D Appl. Phys.* **42**, 165204 (2009)
15. B. Öktem, I. Pavlov, S. Ilday, H. Kalaycıoğlu, A. Rybak, S. Yavaş, M. Erdoğan, F.Ö. Ilday, *Nat. Photon.* **7**, 897–901 (2013)
16. S. Kawata, H.-B. Sun, T. Tanaka, K. Takada, *Nature* **412**, 697–698 (2001)
17. K. Dickmann, J. Jersch, F. Demming, *Surf. Interface Anal.* **25**, 500–504 (1997)
18. S. Huang, M. Hong, Y. Lu, B. Lukázanchuk, W. Song, T. Chong, *J. Appl. Phys.* **91**, 3268–3274 (2002)
19. B. Wang, L. Gallais, *Opt. Express* **21**, 14698–14711 (2013)
20. K.-S. Kim, Q. Zou, *IEEE/ASME Trans. Mechatron.* **18**, 1767–1777 (2013)
21. K. Soong, R. Byer, C. McGuinness, E. Peralta, E. Colby, *Experimental determination of damage threshold characteristics of IR compatible optical materials. Particle Accelerator Conference Proceedings* (2011), p. 277